Generating Locomotion with Effective Wheel Radius Manipulation

Tim Hojnik[1,2], Lachlan Pond[1,2], Ross Dungavell[1], Paul Flick[1], Jonathan Roberts[2]

Abstract— **Travel over sloped terrain is difficult as an incline changes the interaction between each wheel and the ground resulting in an unbalanced load distribution which can lead to loss of traction and instability. This paper presents a novel approach to generating wheel rotation for primary locomotion by only changing its centre of rotation, or as a complimentary locomotion source to increase versatility of a plain centre hub drive. This is done using linear actuators within a wheel to control the position of the centre hub and induce a moment on the wheel from gravity. In doing so our platform allows for active ride height selection and individual wheel pose control. We present the system with calculations outlining the theoretical properties and perform experiments to validate the concept under loading via multiple gaits to show motion on slopes, and sustained motion over extended distance. We envision applications in conjunction to assist current motor drives and increasing slope traversability by allowing body pose and centre of gravity manipulation, or as a primary locomotion system.**

Fig. 1: Experimental setup of wheels mounted to a chassis, manipulating their effective radii to manipulate the centre of gravity and generate locomotion on an 8° (14% gradient) angle of inclination.

I. Introduction

Wheels provide a very low Cost Of Transport (COT) transport solution due to their geometric shape providing continuous ground contact on smooth terrain [1]. Suspension system are generally added to maintain desired ground traction on uneven terrains. It is common to see rigid-wheels mounted to a variety of systems such as automated guided vehicles (AGVs) for manufacturing and exploration tasks [2]. Further, a significant focus of wheels has been for extra-terrestrial rover design for traversing natural terrain [3].

The majority of these systems utilise a rigid-wheel with suspension [4], and have limited body pose control or active wheel adjustment capabilities. An example of a limitation of such systems is the NASA Spirit Mars rover that became stuck in a sand trap in late 2009, as the only pose control it possesses is angular velocity control of its wheels [3].

A variety of alternative locomotion systems have been proposed. One design is a spatially variable origami wheel designed to offer variable torque in a small, lightweight and passive system [5]. This system offers continuous torque adjustment by deforming the wheels and reducing their diameter as a torque load is applied. Others propose a shape-changing wheel [6] that generates locomotion by changing its external shape to eliminate the need for drive trains and motors, greatly reducing the overall complexity and size.

Similarly, a system using deformable wheels and hybrid actuators with smart structures and composite flexure linkages [7] has been proposed. It deforms its wheels to generate locomotion and can in turn navigate small spaces by spatially adjusting its wheel footprints. Another approach proposes discrete steps by using polygons (and polyhedrons) in which the accelerations of edge lengths are controlled to cause tipping motions over desired vertices [8].

Further from the wheeled system, snake-like locomotion for exploration [9] and dynamic locomotion via shape shifting walking, crawling and rolling robot [10] are proposed for applications such as urban reconnaissance and surveillance.

These approaches tackle locomotion differently, however COT is lowest with traditional wheeled systems, although lacking configurability like others, to allow movement through dynamically changing terrains [11]. Our system can act as a passive wheel to inherit the low COT and structural integrity of traditional systems, or when desired, exhibit dynamic centre hub positional control to allow vehicle pose control and provide an alternative locomotion system using gravity to generate a moment about its axles.

The major contribution of this research is functional method for chassis pose control, by changing the effective radius of wheels. This allows for the manipulation of the platform Centre Of Gravity (COG), which can generate locomotion using gravity or compliment a motor drive. This can be used to add extra torque to the motors, using gravitational potential energy. Secondly, slope traversability is increased as the COG can be lowered and shifted uphill. Preventing traction losses or vehicle rollovers and maintaining the desired ground contact with all wheels.

Our system can overcome the current limitations of traction loss and instability for travel on slopes. This is critical for terrestrial and extra-terrestrial rovers and platforms designed for hill climbing as it increases their usability. Uses that require robot body pose control such as sensitive payload transport are also perceived to benefit from this research.

[1]with Cyber-Physical Systems, Commonwealth Scientific and Industrial Research Organisation (CSIRO), Brisbane. {name.surname@csiro.au}.

[2]with the Science and Engineering Faculty, Queensland University of Technology (QUT), Brisbane, Australia. {name.surname@qut.edu.au}.

II. Mechanical Design

We propose a wheel with a centre hub that is actuated independently to the outer rim, on a plane perpendicular to the axle. Our current implementation uses pneumatic actuation and electrical actuation is currently being explored. The design aims to provide a posable hub with benefits of large travel suspension in the restricted volume of the wheel.

A. Active Wheel

The wheel used in this paper is a three degree of actuation (DOA) system developed from earlier research described in paper [12]. The wheel makes use of a rigid rim and centre hub, mechanically coupled with three pneumatic cylinders. The coupling mounts are designed to mechanically restrict the motion of the hub within a plane, resulting DOA are in x, y and θ rotational about z axis. This allows the wheel to be locked into a passive state when desired and act as a traditional wheel, maintaining its low cost of transport.

These pneumatic cylinders coupling the rim and hub are actuated by controlling the airflow via a solenoid valve [13], controlled by an onboard microcontroller that receives high level commands from an external computer. Inverse kinematic control of the centre hub with respect to a point on the rim is used, to allow positional control throughout the wheels full rotation. Each wheel is supplied with pressurised air, power and a communications line. These three tethers to the external world are daisy chained together to minimise the number of connections to the system.

B. Chassis

The chassis is shows in Figure 2 and consists of a rigid cross-member providing in-line mounting points for two wheel axles. The wheel axles are mounted onto the chassis in parallel, as a bicycle, spaced a sufficient distance apart to ensure the wheels can move without colliding when the effective radius is changed. A caster wheel was added to the cross-member in order to support and balance the system on a smooth surface such as a wall. The two active wheels support all the weight and control the ride height and weight distribution, while the caster wheel rests against a wall, maintaining the chassis upright.

C. Data Collection

Data collection consisted of wheel rotation and chassis height collection attached to an Arduino and Matlab to determine the motion characteristics of the generated motion.

The rotation of each wheel is recorded using a quadrature rotary encoder at 100Hz and resolution of 600 increments per full rotation. This high resolution was needed as the large wheel radius results in large ground travel increment for each rotational increment.

Each wheel mounting point also has a ground time-of-flight laser sensor utilised as a ride height sensor. This sensor measures the instantaneous distance between the centre of the wheel and its contact patch and was time-stamped to allow data analyses in conjunction with the rotation of the wheel sensor.

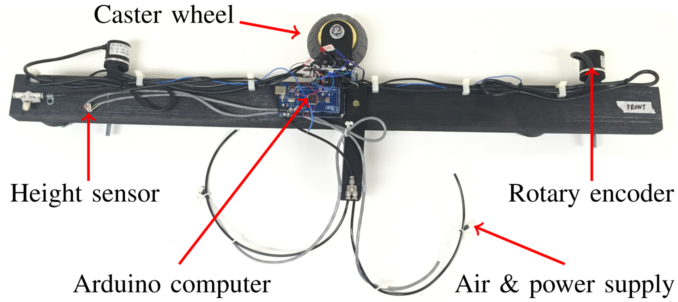

Fig. 2: Chassis used to perform the experiments. A caster wheel was used to stabilise the platform, rotary encoders on each wheel to record rotation and time of flight sensors to record ride height.

III. Definitions and Assumptions

To aid in calculations, certain assumptions and reference frame simplifications were made when describing the system.

A. Frames of Reference

The main reference frames used are the centre hub F_H frame which is fixed to the nominal centre of the wheel but does not co-rotate with the wheel. A secondary frame F_C is fixed to the nominal centre of rotation of the wheel, where F_H moves with respect to X_C and Y_C as the effective wheel radius is changed. Frame F_B is the wheel body frame that is fixed to a point on the rim, with its Y_B axis pointing through the origin of F_C and is used to measure the effective wheel radius. The overall wheels and chassis move in an inertial frame F_I and the frame F_K is fixed to the COG of the chassis under nominal conditions. F_C is used to describe the wheel positions with respect to the chassis. These wheel and chassis frames are shown in Figure 3.

B. Ground Contact and According Assumptions

1) Rolling Assumptions: A pure rolling assumption, later validated, is made for this work with the wheel exhibiting no slip with its contact surface. A rubber tyre was used with an off-road tread pattern to maximise traction and prevent energy loss through slip. This resulted in

$$a = r\alpha \tag{1}$$

holding true. Where a is linear acceleration, r is the effective radius and α is the angular acceleration of the wheel.

2) Contact Patch: The contact patch is characterised by the contact area each wheel makes with the ground. Calculated by dividing the single wheel load L_w by the tire inflation pressure IP as follows

$$CP = \frac{L_w}{IP}. \tag{2}$$

The centre of the single point in contact with the ground has a velocity of $0ms^{-1}$ as it does not move relative to the ground while in contact, to satisfy Equation 1. Equation 2 allows for the contact patch area to be know in order to predict if slip will be present on different terrains.

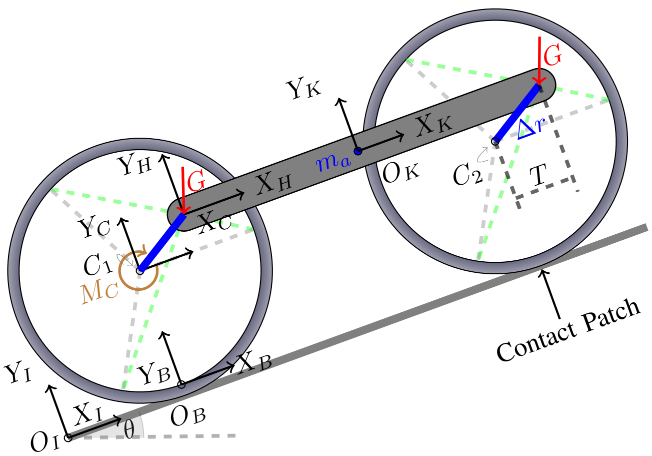

Fig. 3: Gray dotted lines show the nominal actuator positions and green shows actuators at manipulated distance Δr. Gravity acts on this point producing M_C about point C, generating locomotion upwards on slope inclination angle of θ.

3) Static Nominal Ground Pressure: The static wheel contact pressure is a ratio between the weight and contact patch of the system, used to determine the system suitability for specific environments [14] and can be found by

$$NGP = \frac{L_w}{rW_w}. \tag{3}$$

L_W is the wheel load, r is wheel radius and W_W is the width of the wheel. This is important as it directly contributes to the contact patch calculation. However, this method neglects the impact of tire deflection under load and during movement, tire air pressure and independence on ground characteristics [15].

4) Coefficients of Friction: The coefficient of static friction is equal to the tangent of the angle at which the wheel began to slide, and the dynamic equal to the angle of which the wheel maintained a consistent slide [16]. The angles were recorded from the experimental setup and μ calculated using

$$\mu_s = tan(\phi_s), \tag{4}$$
$$\mu_k = tan(\phi_k), \tag{5}$$

which yielded $\mu_s = 0.95$ and $\mu_k = 0.8$. These values were used to represent the experimental environment.

IV. Platform Modelling and Validation

Modelling of the platform is developed to determine its properties and traversability on varied slopes.

A. Platform Stability on a Slope

When the platform is at rest on an incline θ, the front C_1 and rear C_2 axle loading varies based on θ and chassis design. If the platform with weight M has a COG with vertical distance h from the ground, x_f is the offset between the COG and front wheel and W_B is the wheelbase, the wheel loading can be found using

$$R_R = \frac{M}{W_B}\Bigg((W_B - x_f 0cos(\theta) - hsin(\theta)\Bigg), \tag{6}$$
$$R_F = \frac{M}{W_B}\Bigg((x_f cos(\theta) + hsin(\theta)\Bigg). \tag{7}$$

As the angle θ increases one of two situation can occur; the platform can stay in its statically stable state, or become unstable and overturn. This limiting angle θ_L is found by

$$\theta_L = tan^{-1}\Bigg(\frac{W_b - x_f}{h}\Bigg). \tag{8}$$

B. Angular Acceleration

The angular acceleration of the wheel defines the overall wheel acceleration. As the acceleration is proportional to the mass moment of inertia (Equations 13 & 14), an equation is derived for each configuration using the torque equation

$$\tau_{net} = I\alpha. \tag{9}$$

Substituting values common to both wheels states yields

$$mgcos(\theta)r = I_i\alpha \quad \forall i. \tag{10}$$

Rearranging for α, and substituting equation 13 and 14 respectively gives the final accelerations of the wheel states

$$\alpha_{nominal} = \frac{2\mu gcos(\theta)r}{(R_1^2 + R_2^2)}, \tag{11}$$

$$\alpha_{manipulated} = \frac{2\mu gcos(\theta)r}{(R_1^2 + R_2^2) + \Delta r^2}. \tag{12}$$

C. Mass Moment of Inertia

The mass moment of inertia (I) of an angular cylinder about its central axis standard formula

$$I_N = \frac{M}{2}(R_1^2 + R_2^2), \tag{13}$$

yields the moment of inertia of this wheel in its normal state. Actively manipulating the wheel radius to shift mass however changes the moment of inertia. The parallel axis theorem can be used to determine the new value and states that $I = I_{cm} + md^2$, where I_{cm} is the body moment of inertia with respect to an axis, I is the new moment of inertia offset by distance d from I_{cm} axis. The new I_E is then given by

$$I_E = \frac{M}{2}(R_1^2 + R_2^2) + m\Delta r^2. \tag{14}$$

D. Centre of Gravity

1) Wheel: The centre of gravity on the $x-y$ plane of each wheel is modelled to be directly proportional to its normal radius. Under nominal circumstances the wheel radius is equal in x and y, as a result its COG is the geometric centre of the wheel. COG in z direction is modelled as proportional to the wheel thickness W_T. For all points in hub workspace H_W calculated by Equation 25, in reference frame F_H, where $R_x \equiv R_y \equiv R_n$ the COG is simply

$$COG = \{R_x, R_y, W_T/2\} \,/\, Rx, Ry \in H_W \tag{15}$$

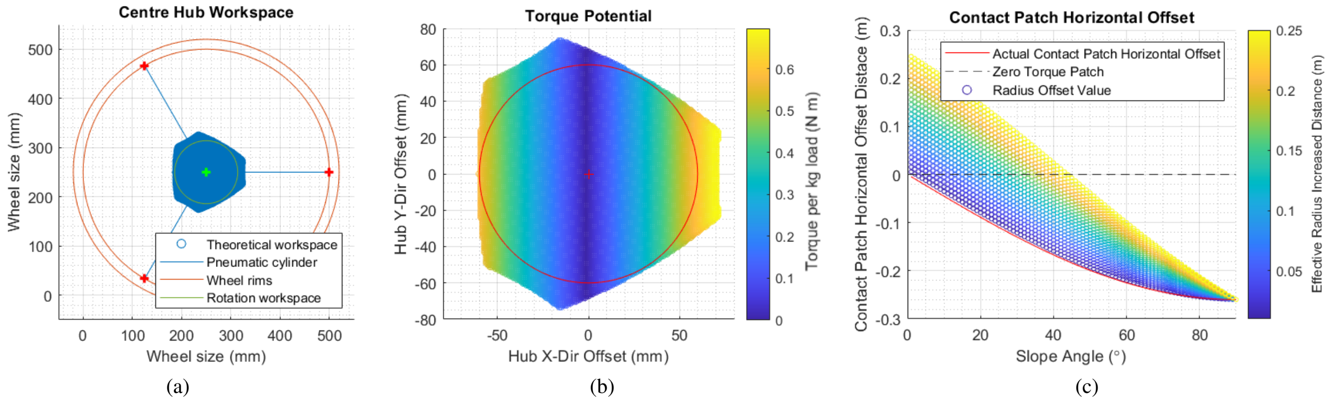

Fig. 4: (a) Shows the centre hub workspace inside the wheel. (b) Shows the torque able to be generated at each point where Hub X-Dir Offset is demonstrated by T in Figure 3. (c) Shows the slope angle (θ) able to overcome for varying radius change (Δr) wheels.

Upon actuation, the wheel radius changes unevenly from the centre point $R_x \neq R_y$, the centre of gravity is then given by

$$COG = \{\Delta r, \cos(\psi) - R_n, W_T/2\} \,/\, COG_{x,y} \in H_W \quad (16)$$

2) Chassis: Likewise, COG of the chassis is assumed to be in its geometric centre due to symmetry. As the effective radius of the wheels W change, it can then be found using

$$COG_{x,y} = -(COG_{x,y}(W_1) + (COG_{x,y}(W_2)), \quad (17)$$

$$COG_z = -(COG_z(W_n) + (W_C/2)). \quad (18)$$

Where W_n is any of the wheels used on the systems.

E. Gravitational Moment Generating Torque

The chassis load induces a moment as it acts through a single point of each wheel, at its axis. This point, C, is shown on Figure 3 and the moment about it is found using

$$M_C = gm\Delta r sin(\theta). \quad (19)$$

When the wheel is in its normal configuration $\Delta r = 0$, all the forces act through the point C, therefore no moment is induced in the wheel. As Δr increases, a greater moment acts about point C, the different torque potential of different points is shown in Figure 4b. The maximum rotation of the wheel due to M_C can also be calculated using

$$R_{max} = 90° + \theta, \qquad -90° < \theta \leq 90° \quad (20)$$

and the maximum distance the wheel can in turn travel using

$$D = 2\pi r * \frac{R}{360}. \quad (21)$$

F. Gravitational Potential Energy

The gravitational potential energy, with respect to the ground, of the wheel can be calculated using

$$U = gm\Delta R_y \quad (22)$$

where ΔR_y is known for each control point. Equations 19, 20, 21 show that when the hub is offset at $\theta = 90°$, the wheel benefits from highest potential energy, however the system is unstable. At this point the moment is zero, but a minor disturbance[1] will cause the moment to greatly increase until the wheel preforms an under-damped rotation of 180° and loses its potential energy as the weight settles at the most stable point.

[1] Which is expected in the real world such as wind or residual movement.

G. Theoretical Traversable Slope Angle

The maximum traversable slope angle by pure use of gravity can be determined using trigonometry. Referring to Figure 3, θ denotes the slope angle where θ_{max} is the maximum traversable slope angle calculated using

$$\theta_{max} = 90 - tan^{-1}\left(\frac{R}{\Delta r}\right). \quad (23)$$

Where Δr is found by

$$\Delta r = \sqrt{R_e^2 - R^2}. \quad (24)$$

The maximum traversable slope angle is then $(\theta_{MTSA}) < \theta_{max}$. This calculation is shown in Figure 4c for a number of wheels with different maximum Δr values, for comparison.

Figure 3 further shows point C as the true centre of the wheel, and the corresponding dashed red lines denote the cylinder positions to achieve this. Point D shows the manipulated position to generate moment M_C about point c. Cylinder positions for D are denoted by green dashed lines.

H. Centre Hub Workspace within the Wheel

The number of control pistons and their minimum and maximum reach directly impacts the wheel and the workspace available to the centre hub. The range of motion of the hub was found by generating a number of points and testing to determine if they were kinematically realisable. This allowed simple limit theory to determine the wheels workspace for specific piston configuration. A point lies within the workspace if it satisfies the following condition for all the pistons (i):

$$PR_{min} \leq \vec{P_i} \leq PR_{max}, \qquad \forall i \quad (25)$$

where $\vec{P_i}$ is the modelled piston vector spanning from P_i to D, PR_{min} and PR_{max} are the minimum and maximum reach of the pistons, respectively. The workspace points are

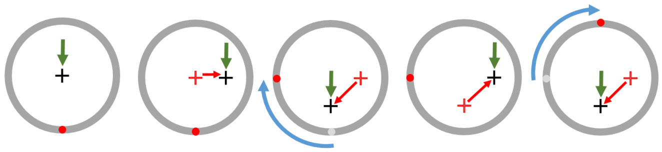

Fig. 5: Normal rolling gait. Green shows the force of gravity, red point on the outer rim shows rotation and blue arrow shows the torque generated by gravity at the offset centre position. Black and red crosses show current and past centre of rotation, respectively.

then represented as a vector H_W of reachable x and y points. The calculated workspace is shown in Figure 4a in blue. However, as the workspace has a reuleaux triangle shape, the minimum radius vector on the reuleaux triangle to the centre hub yields the radius of the usable rotational workspace of the wheel. This is shown in the green circle, and ensures any point within the green circle is kinematically realisable irrespective of instantaneous wheel rotation.

V. Experimental Validation

Experiments conducted in this paper focused on showing controlled manipulation of the wheel centre hubs in order to generate motion. Sustained motion is shown on level ground and slope climbing at different gradients. The proof-of-concept was validated in a controlled environment with concrete floor and the sloped angles created using a plank of wood to provide sufficient traction with the wheel and eliminate slip. This experimental setup is shown in Figure 1.

A. Start-up Gait

The start-up gait was required for all gaits in order to offset the hub from its geometric centre of rotation to a unstable position able to generate torque using the extra potential energy in the system. The magnitude of this lateral position change can be determined by the amount of torque required to initiate rotation, torque acheivable at each position is shown in Figure 4b. Figures 5a, b show this gait.

B. Pump Gait

The pump gait consists of moving the centre hub in the direction of desired motion, letting the wheel rotate due to gravity and settle, then moving the centre position again to repeat this rotation. This gait requires the start-up gait to first be performed then steps shown in Figure 5c to Figure 5e to be repeated to maintain a pump-like forward motion.

The pump gait was used on flat terrain and tested on slopes, data is presented in Figure 6. Figure 6a specifically shows this gait performed on a flat surface, and highlights the smooth relationship between the hub vertical position (ride height) and the rotation of the wheel. As the ride height is at its maximum (Figure 5b) the system has the greatest potential energy due to gravity. Once rotation is initiated by actuation to an unstable state, the wheel turns and converts its ride height to angular velocity. When the ride height reaches its minimum (Figure 5c) there is no gravitational energy left in the system, and it comes to a critically damped stop as the rotational energy is lost to friction.

TABLE I: Slope angles and corresponding average velocity of the wheel achieved during the experiments performed.

Figure	Slope (°)	Gradient (%)	$\omega_{avg}(°s^{-1})$	$V_{avg}(ms^{-1})$
6a	0	0	428	2.278
6b	3	5.24	142	0.756
6c	5	8.75	123	0.655
6d	8	14.05	50	0.266

Figures 6b, 6c and 6d also show the gate being used for slopes of $3°$, $5°$ and $8°$, respectively. The relationship between wheel rotation and ride height in these figures is less coherent as Figure 6a, due to extra forces acting on the system and a trade off between local potential energy of the hub and the potential energy gain of the whole system as it climes the slope. The results show the platform developing a lateral tilt, seen in the difference in ride height of the front and rear wheels, as it drives on the slope which in turn displaces the COG and the locomotion becomes less efficient. Table I shows the slopes and angular velocities of the wheels achieved during the performed experiments.

C. Sustained Driving Gait

The sustained driving gait is achieved by continuous centre hub adjustment to maintain a set ride height. Start-up gait is required to introduce the initial energy into the system and initiate rotation. The gait requires continuous readjustment of the centre hub and as a result requires more energy to generate motion, however provides smoother driving for the platform than the pump gait as it maintains a set ride height.

The period of control for the hub position depends on a number of factors. As the speed of rotation increases, the control frequency has to follow to maintain smooth driving. This can be set in the controller that reads the rotation and the ride height, then determines if a new position is required based on the allowed ride height deviation.

The ride height of the wheel can be set to be lower or higher than its geometric centre of rotation, based on the amount of torque required. The set ride height is directly proportional to the gravitational potential energy in the system and the potential energy conversion into torque is controlled by the lateral position of the hub.

Figure 7 shows the ride height data plotted verses rotation of the wheel recorded over an 8.5metre drive. The figure shows a number of small disturbances on the ride height of the platform, with a standard deviation from the mean ride height of $\pm 4.5mm$. Both the front and rear wheel of the system maintained a desired ride height with minimal error, while generating locomotion over a sustained distance, validating that this is an effective locomotion system.

VI. Discussion

The posable hub system performed well on a level surface by converting the gravitational potential energy, through inducing a moment on the wheels, to rotational wheel motion. Figure 6a shows the smooth transitional relationship between wheel rotation and the gravitational potential energy in the form of ride height. Figure 7 further validates this method over a sustained driving distance of 8.5 metres.

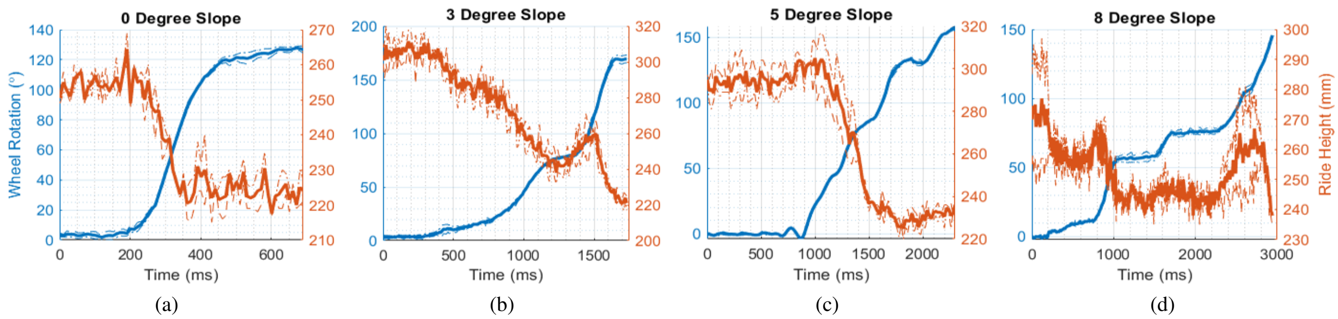

Fig. 6: Wheel rotation generated using the pump gait. (a) shows the platform motion on a level surface, (b) on a 3° (5.2% gradient), (c) a 5° (8.7% gradient) and (d) an 8° (14% gradient) incline. The tyre made contact with a smooth wooden surface at a chosen slope angle.

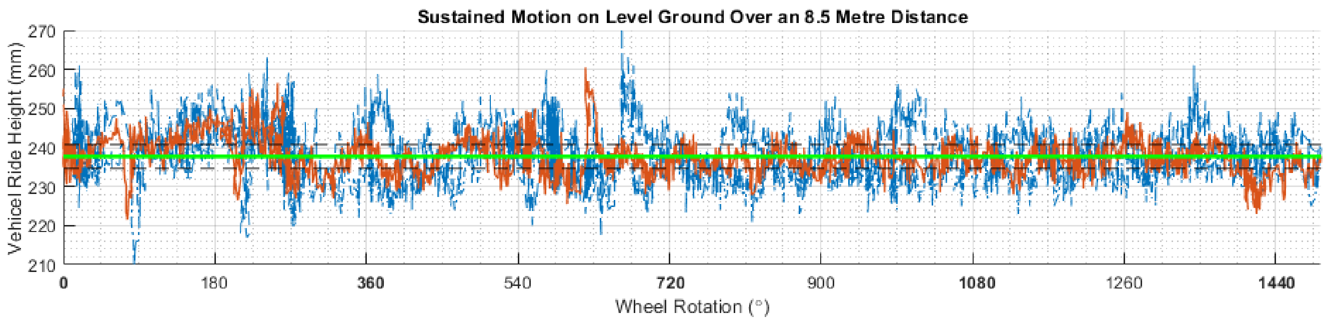

Fig. 7: Data recorded during sustained rotation of the wheel over an 8.5 metre distance, using the sustained driving gait discussed in Section V-C. A 24 inch diameter wheel was used which travelled 1.92 metres for each full rotation, figure shows ≈ 4.5 full rotations.

This system was tested on a variety of slopes until a maximum traversable slope was reached, at which point the trigonometric configuration did not allow any moment to be generated. The theoretical maximum traversable slope angle calculated in Section IV-G and shown in Figure 4c was found to be 12°. Experimentally, using the pump gait, a maximum traversable slope angle of 8° was achieved. Therefore, 67% of the theoretical angle was able to be achieved in practice before the system began experiencing difficulties in moving up the slope. The calculations assume a perfect world model, with no friction between the wheel components and perfect actuator positions. This is incorrect in the physical testing environment and evident in the experiments.

Friction between the wheel, surface and in the actuators contributed to a loss in energy, coupled with the less-than-perfect horizontal weight distribution and other losses in wheel bearings, all contributed to the physical performance of the system. The locomotion on slope angles achieved are however, sufficient to prove this locomotion system functions as envision on the early prototype system.

One inherit benefit of the posable hub wheels provided sufficient control to adjust their ride heights, and maintain a level chassis on the slope. Although no motor was present to then drive the wheels up a steeper incline than 8°, this validated the systems ability to control the body pose. A traditional systems such as the rocker bogie configuration [17] for sloped terrain, cannot provide any active body pose control, therefore may not be as suitable for sensitive payload transport over uneven and sloped terrain.

The pneumatic actuators used in the wheel functioned sufficiently to demonstrate the wheel functions, however lacked smooth control. Pneumatic were used for this initial prototype as they demonstrate compliance due to the underlying properties of air. This compliance was able to absorb vibration and bumps encountered by the system, and act as a suspension system for the robot. However, due to the complexity of pneumatic and their incompatibility for use in environments lacking a sufficient atmosphere, electric actuators are being explored as a replacement. It is important to note that this system can function with a variety of actuators such as pneumatics, electric, hydraulic or mechanical actuation, each suited to a specific application.

VII. Conclusion and Future Work

We propose a novel locomotion system for mobile robots that converts gravitational potential energy into rotational motion to increase slope traversability. We model the system to estimate performance and evaluate its applications based on the calculations. Experiments were performed with two wheels mounted to a chassis and validated the system. Maintained motion on flat ground and slopes was achieved however, physical forces such as friction had a sizeable impact on the performance. Another drawback was the lack of rigidity due to 3D printed components, and difficulty in maintaining driving in a straight line. Oscillation from the pneumatic cylinders was also encountered. Future work will focus on optimising the controller and building a new chassis to minimise the energy losses and increase rigidity as well as development of electric actuators to replace pneumatics. In doing so, other wheel and chassis configurations can also be built to maximise the traversable slope angle and demonstrate further benefits of our locomotion system.

REFERENCES

[1] Feng Ren, Longhai Li, Zhengying Jiang, Tao Song, Xun Gong, Yaowu Shi, and Boliang Liu. Analysis on wheel–ground contact load characteristics of unmanned off-road vehicles. *Journal of Engineering Science & Technology Review*, 10(3), 2017.

[2] Hee-Woon Cheong and Hwally Lee. Requirements of agv (automated guided vehicle) for smes (small and medium-sized enterprises). *Procedia computer science*, 139:91–94, 2018.

[3] Randel A Lindemann and Chris J Voorhees. Mars exploration rover mobility assembly design, test and performance. In *2005 IEEE International Conference on Systems, Man and Cybernetics*, volume 1, pages 450–455. IEEE, 2005.

[4] Ioan Doroftei, Victor Grosu, and Veaceslav Spinu. *Omnidirectional mobile robot–design and implementation*. INTECH Open Access Publisher, 2007.

[5] Dae-Young Lee, Gwang-Pil Jung, Min-Ki Sin, Sung-Hoon Ahn, and Kyu-Jin Cho. Deformable wheel robot based on origami structure. In *2013 IEEE International Conference on Robotics and Automation*, pages 5612–5617. IEEE, 2013.

[6] Daniel Mellinger, Vijay Kumar, and Mark Yim. Control of locomotion with shape-changing wheels. In *Robotics and Automation, 2009. ICRA'09. IEEE International Conference on*, pages 1750–1755. IEEE, 2009.

[7] Je-sung Koh, Dae-young Lee, Seung-won Kim, and Kyu-jin Cho. Deformable soft wheel robot using hybrid actuation. In *2012 IEEE/RSJ International Conference on Intelligent Robots and Systems*, pages 3869–3870. IEEE, 2012.

[8] Woo Ho Lee and Arthur C Sanderson. Dynamic rolling locomotion and control of modular robots. *IEEE Transactions on robotics and automation*, 18(1):32–41, 2002.

[9] Alessandro Crespi, André Badertscher, André Guignard, and Auke Jan Ijspeert. Amphibot i: an amphibious snake-like robot. *Robotics and Autonomous Systems*, 50(4):163–175, 2005.

[10] Takeru Yanagida, Rajesh Elara Mohan, Thejus Pathmakumar, Karthikeyan Elangovan, and Masami Iwase. Design and implementation of a shape shifting rolling–crawling–wall-climbing robot. *Applied Sciences*, 7(4):342, 2017.

[11] M Bozic, N Ducic, G Djordjevic, and R Slavkovic. Optimization of wheg robot running with simulation of neuro-fuzzy control. *International Journal of Simulation Modelling (IJSIMM)*, 16(1), 2017.

[12] Tim Hojnik, Paul Flick, Tirthankar Bandyopadhyay, and Jonathan Roberts. Dynamic manipulation of gear ratio and ride height for a novel compliant wheel using pneumatic actuators. In *2019 IEEE International Conference on Robotics and Automation*, pages 987–992. IEEE, 2019.

[13] Tim Hojnik, Paul Flick, and Jonathan M Roberts. Contactless position sensing and control of pneumatic cylinders using a hall effect sensor array. In *Robotics and Automation. Australasian Conference on*, 2017.

[14] Tomislav Poršinsky, Tibor Pentek, Andreja Bosner, and Igor Stankić. Ecoefficient timber forwarding on lowland soft soils. In *Global Perspectives on Sustainable Forest Management*. IntechOpen, 2012.

[15] M Saarilahti et al. Soil interaction model. manual 1. seltra. documentation of the computer programme for calculating of the trafficability of terrain and the mobility of forest tractors. Technical report, 2002.

[16] EJ Berger. Friction modeling for dynamic system simulation. *Applied Mechanics Reviews*, 55(6):535–577, 2002.

[17] Moshe P Mann and Zvi Shiller. Dynamic stability of a rocker bogie vehicle: Longitudinal motion. In *Proceedings of the 2005 IEEE international conference on robotics and automation*, pages 861–866. IEEE, 2005.